Rock Mechanics and Rock Engineering (2025) 58:623–644
https://doi.org/10.1007/s00603-024-04165-1

ORIGINAL PAPER

Hydro-Grain-Texture Modeling of Systematics of Propagation, Branching, and Coalescence of Fluid-Driven Fractures

Suifeng Wang[1] · Derek Elsworth[2] · Liping Zhang[1] · Xianyu Zhao[3] · Tao Wang[1]

Received: 24 April 2024 / Accepted: 1 September 2024 / Published online: 24 September 2024

Abstract

The heterogeneity of the mineral grain structure and presence of pre-existing flaws significantly impacts fracture propagation within amorphous crystalline rocks. We explore the macro-mechanical response derived from microfracture evolution for fluid-driven fracturing (hydraulic fracturing) in a granite with pre-existing flaws. We introduce a hydro-grain-texture model (HGTM) based on a "grain growth" algorithm that accurately characterizes the microscale granular structure of minerals subject to the influence of driven fluids. The single and double flaws of different geometries are introduced to investigate hydraulic fracture propagation in granites under combined influence of heterogeneity and anisotropy. The results demonstrate that the HGTM can consistently reproduce the principal features of fracture propagation and coalescence observed in experiments. It is found that the hydraulic fracturing results (fracture number, type, and tortuosity) and breakdown pressure are affected by the interactions of confining stress, mineral heterogeneity, and flaw geometry. Confining stress induces the extension of fluid-driven fractures in the direction of the maximum principal stress. While with absence of confining stress, fractures tend to extend along the long axis of the flaw and are more susceptible to grain boundaries and breakdown pressure is also primarily determined by the local strength at the flaw tip. In double flaw specimens, both the flaw bridging angles and confining stress jointly influence the patterns of fracture propagation and coalescence.

Highlights

- A novel hydro-grain-texture model (HGTM) is proposed to investigate the hydraulic fracturing behavior of crystalline rock.
- The combined influence of mineral heterogeneity, confining stress condition, and flaw geometry on hydraulic fracturing is investigated.
- Fluid-driven fracturing propagation, branching, and coalescence in granite containing single and double flaws are reproduced.
- The fracture tensile failure mode mechanism in hydraulic fracturing test is investigated.

Keywords Hydraulic fracturing · Hydro-grain-texture model · Pre-existing flaws · Mineral heterogeneity · Breakdown pressure

✉ Tao Wang
htwang@whu.edu.cn

[1] State Key Laboratory of Water Resources Engineering and Management, Wuhan University, Wuhan 430072, China

[2] Department of Energy and Mineral Engineering, EMS Energy Institute and G3 Center, Pennsylvania State University, University Park, PA, USA

[3] College of Hydraulic and Environmental Engineering, China Three Gorges University, Yichang 443002, China

1 Introduction

Deep geothermal energy offers potential as a zero-carbon and sustainable source of power. Key challenges remain in creating and sustaining permeable networks of fractures in the initially micro-darcy or lower permeabilities of these potential reservoirs (Zang and Stephansson 2010). Enhanced geothermal systems (EGS) are specifically designed to

enhance fluid conductivity within low-porosity hot dry rock (HDR) reservoirs by hydraulic fracturing with cold water create fracture networks (Adachi et al. 2007; Zang et al. 2014). However, the process of fracturing crystalline rocks such as granites for geothermal energy remains a challenge (Zhuang and Zang 2021; Zhuang et al. 2022). The challenge associated with granites stems from their heterogeneity and anisotropy.

The heterogeneity and anisotropy in the mechanical properties of granite are primarily attributed to two factors. Firstly, its mineral microstructure, including mineral size, shape, and composition, results in conspicuously brittle characteristics due to the inter-locking characteristics of the minerals (Lan et al. 2010; Hofmann et al. 2015; Peng et al. 2017, 2021). Secondly, granite contains numerous flaws at various scales (such as microcracks, joints, and faults) that significantly impact its mechanical properties and fracturing behavior (Ji et al. 2021; Naoi et al. 2020). To investigate the influence of these factors on fracture initiation, propagation, and coalescence, extensive uniaxial compression tests have been conducted on granite specimens containing prefabricated flaws. These include uniaxial compression tests on granite and gypsum specimens containing single flaws (Wong and Einstein 2009a). By employing scanning electron microscope (SEM) and high-speed cameras, they identified seven modes of crack initiation (wing crack; anti-wing crack; coplanar secondary crack; oblique secondary crack; out-of-plane tensile crack; out-of-plane shear crack; far-field crack) from flaws and proposed that the mineral structure of rocks significantly influences the fracturing process (Fig. 1). Uniaxial compression tests on rocks containing double and multiple flaws (Bobet and Einstein 1998; Wong and Einstein 2009b, c; Cheng et al. 2016) have explored fracture types. It is important to note that there are significant differences in loading conditions between uniaxial compression and hydraulic fracturing, leading to variations in the processes of crack propagation and coalescence (Gonçalves 2016). Hydraulic fracturing tests on granite specimens with double pre-existing flaws have examined fluid-driven fracturing in granite through direct observation, acoustic emission monitoring, SEM, high-speed cameras, and comparing observations with those from uniaxial compression tests (Li and Einstein 2019; Li et al. 2015; Gunarathna and Gonçalves 2019, 2021; Gonçalves 2016; Gonçalves and Einstein 2018). However, numerical studies of processes on granite with pre-existing flaws are still lacking—the topic of this contribution.

While experiments provide the most direct approach to investigate the mechanical and fracturing behavior of rocks, they are also accompanied by inherent limitations. The observation of microfracturing behavior in rocks during experiments poses a particular challenge (Sagong and Bobet 2002). Furthermore, the characterization of microscopic features such as microfractures using SEM demands a substantial investment of time and effort (Cheng and Wong 2018). Therefore, the development of precise numerical models for accurately depicting the microscopic characteristics of rock and fluid–solid coupling offers a viable alternative approach to simulate the mechanical properties and hydraulic fracturing of rock (Cho et al. 2007; Zhao et al. 2021). The discrete element method (DEM) offers a discontinuous mechanical approach for investigating problems from a microscopic perspective, enabling the characterization of fracture generation without being constrained by grid shape (Cundall and Strack 1979; Potyondy and Cundall 2004). Previous studies have made significant progress in simulating hydraulic fracturing using DEM (Wang et al. 2014, 2017; Zhang et al. 2013; Li et al. 2022; Lei et al. 2024). However, despite these

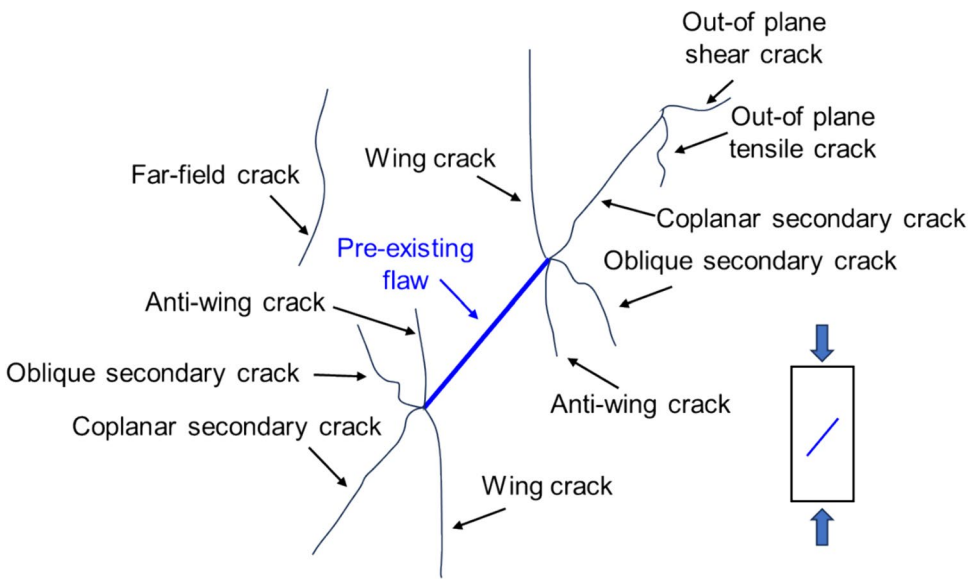

Fig. 1 The crack types observed in rock specimens with pre-existing single flaw obtained from previous experiments (modified from Hu et al. 2023)

advancements, most existing models overlook two crucial aspects: the microstructure of mineral grains and the fragmentation of mineral grains themselves (Zhao et al. 2018; Zhang and Dontsov 2018).

Based on the unique microstructure and mechanical properties of granite, as well as the limitations of current numerical modeling on hydraulic fracturing in granites, we propose a new model—the hydro-grain-texture model (HGTM) based on the DEM. This model integrates a grain-texture model (GTM) and a fluid-domain-pipe model (FDPM). The GTM accurately characterizes the microstructure and mechanical properties of mineral grains using a grain growth algorithm, while the FDPM captures the fluid–solid coupling process in hydraulic fracturing by utilizing particle structures within particle DEM. To comprehensively investigate fluid-driven fracture initiation, propagation, and coalescence, the numerical calculations of hydraulic fracturing are conducted for specimens with varying geometric characteristics with single and double flaws under various conditions of confinement. The combined influence of mineral heterogeneity, confining stresses, and flaw geometry on breakdown and subsequent fracture propagation and coalescence is analyzed. We contrast different cases of hydraulic fracturing with the experimental results to confirm the fidelity of the numerical method.

2 Numerical Modeling Methodology

2.1 Hydro-Grain-Texture Model (HGTM)

The hydro-grain-texture model (HGTM) comprises two primary components: the grain-texture model (GTM) and the fluid-domain-pipe model (FDPM). The GTM can effectively characterize the mineral microstructure and interactions within crystalline rocks (Zhao et al. 2021). The texture of mineral grains in crystalline rocks is governed by both grain boundaries (GB) and intra-grains (IG), collectively determining the mechanical properties of the rocks (Zhang et al. 2024; Zhou et al. 2024). GTM enables differentiation and characterization of grain size as well as grain proportions, thereby facilitating a comprehensive understanding of how different minerals influence macroscale response and elucidating potential behavior mechanisms under diverse conditions. In this study, we conducted numerical simulations using particle flow code software (PFC).

As shown in Fig. 2g, h, the grain-based model (GBM) has been previously employed for the analysis of rock microstructures (Liu et al. 2019; Peng et al. 2018; Kong et al. 2021; Wang et al. 2023). Initially proposed in Potyondy (2010), GBM utilizes a Voronoi tessellation based on particle position to distribute mineral positions and replicate shapes. Despite its extensive application, GBM still has difficulty in representing minerals as fixed convex polygonal shapes and limited ability in assigning multiple mechanical parameters to grain boundaries. These limitations render GBM inadequate in accurately simulating the mechanical properties of brittle rocks, as well as in characterizing morphological changes in mineral grains caused by natural variability. In this work, we employ GTM to characterize the microstructure of crystalline rocks based on grain growth algorithm.

The process of generating numerical specimens through the GTM is illustrated in Fig. 2. This process consists of four steps: (1) random distribution of grain seeds; (2) construction of numerical specimens; (3) definition and expansion of clusters; and (4) identification of contact groups and assignment of mechanical parameters. This workflow accommodates the comprehensive representation and simulation of grain structure, effectively representing

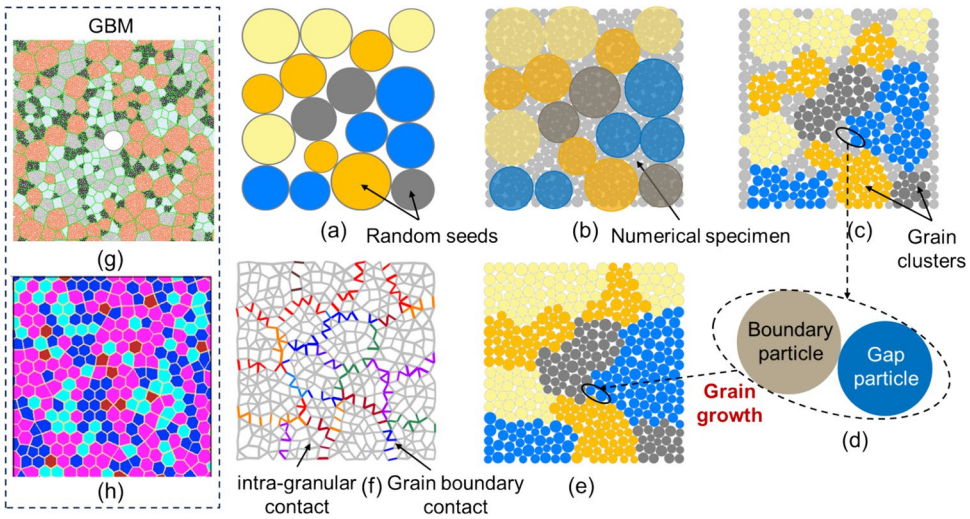

Fig. 2 Generation algorithm for GTM: **a–f** GBM of granite specimen: **g** (Wang et al. 2023) and **h** (Liu et al. 2019)

the diversity of mineral grains and the complexity of their interactions within the model.

The first step in generating numerical specimens through the GTM is illustrated in Fig. 2a, focusing on determining the compositional ratios and sizes of the minerals. By calibrating against target data, particles that mimic specific mineral volumetric fractions and sizes are generated based on random grain seeds. This process establishes a random distribution for grain seeds, providing intricate details on mineral groupings, positions, and sizes of each mineral grain seed. In the second step, as shown in Fig. 2b, a numerical specimen comprising smaller particles is generated. These particles act as elements to the clusters and represent sub-grains sized according to the minimal dimensions of the mineral grains.

Based on the geometric information obtained from the randomly distributed grain seeds, circular clusters are defined within the numerical model. The sub-grains within each cluster are classified into different mineral groups using a classification algorithm that inevitably creates gaps between circular clusters, resulting in some sub-grains being ungrouped and marked as "gap particles" (as shown in Fig. 2c). To address this issue, we then apply a "grain growth" algorithm where clusters expand their boundaries by searching along GB contacts. If a cluster particle encounters a gap particle, it is immediately considered to be a boundary particle defining the boundary of the cluster (as depicted in Fig. 2d). The gap particle is then incorporated into the same mineral group as the boundary particle, thereby extending the grain boundary. This process is repeated until all gap particles are assigned within clusters (as demonstrated in Fig. 2e).

The FDPM proposed by (Cundall and Strack 1979) for simulating fluid flow and hydraulic fracturing. As depicted in Fig. 3, the FDPM generates "fluid domains" and "fluid pipes" based on the spatial distribution of particles, facilitating fluid exchange between these fluid domains. In our previous studies, FDPM has been successfully employed for simulating hydraulic fracturing in coal and shale formations (Wang et al. 2014; 2017). A more comprehensive description of FDPM can be found in Appendix A and our previous studies (Wang et al. 2014; 2017).

2.2 Model Setup

Numerical specimens were created to represent the Pocheon granite from South Korea, which has been extensively studied in previous hydraulic fracturing research (Zhuang et al. 2019; 2020; 2022). The dimensions of the 2D specimens were set at 25 mm for both width and height, with a mixed mineral composition of orthoclase (35.8%), quartz (35.8%), microcline (25.8%), and biotite (2.6%). All mineral grains ranged in size between 0.7 and 1.3 mm, closely resembling

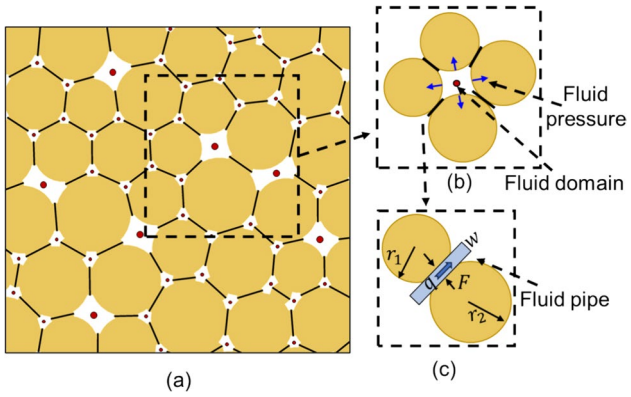

Fig. 3 Schematic of the fluid-domain-pipe model: **a** construction of the fluid network; **b** single fluid domain consisting of four particles (yellow circles are rock particles; area surrounded by particles is fluid domain; black lines are fluid pipes; blue arrows are fluid pressure); **c** fluid pipe between two adjacent particles

the actual Pocheon granite composition reported by Zhuang et al. (2019). Each mineral grain was composed of uniform sub-grains with radii of 0.1–0.166 mm. Two pairs of rigid walls were applied on the specimen boundaries while maintaining constant stress levels throughout the fracturing process by servo mechanism.

As depicted in Fig. 4, this study employed the numerical specimens to investigate the response of single and double flaws with varying assigned orientations, where the flaw length (a) and flaw width were set at 3 mm and 0.15 mm, respectively. In the single flaw model, five models were created with different flaw inclination angles (α). For the double flaws model, the geometric parameters included the flaw inclination angle (α) and bridging angle (β), while maintaining $\alpha = 30°$ and bridging length (b) of 3 mm. The model geometric data used in this study are presented in Table 1.

2.3 Micro Parameters

Intra-grain boundaries in the HGTM utilize the flat-joint model (FJM), while the grain boundary uses the linear parallel bond model (LPBM). The LPBM uses a parallel bonding plate between two particles to describe the mechanical behavior of brittle rocks (Fig. 5a) (Potyondy and Cundall 2004). Potyondy (2018) proposed the FJM, which employs a linear bonding interface between two notional polygonal particles in 2D, allowing a circular particle to mimic a polygonal particle (Fig. 5b). The FJM can realize partial damage by discretizing the bonding interface into different elements. Once the stress exerted on the bonded element exceeds either the tensile or shear strength, the bond will fail in tensile or shear mode. A more comprehensive description of LPBM and FJM can be found in Appendices B and C and our previous studies (Zhao et al. 2021; Wang et al. 2024).

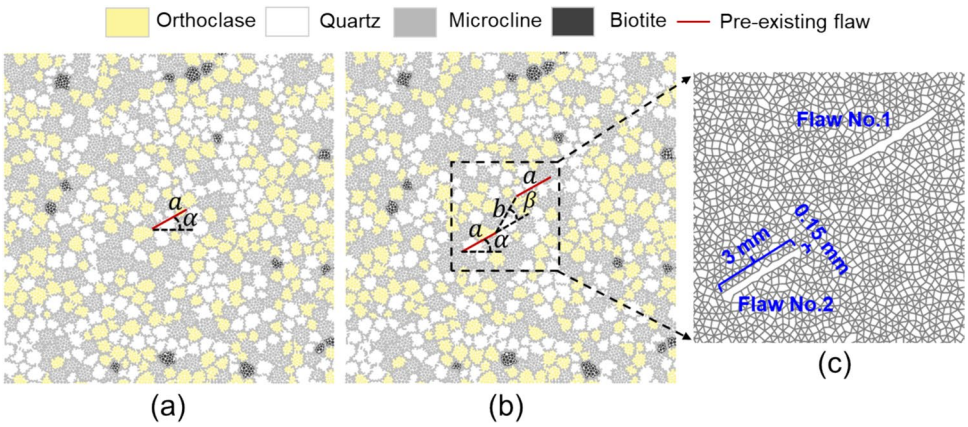

Fig. 4 Numerical specimens containing single and double flaws. **a** single flaw specimen with $\alpha = 30°$; **b** double flaws specimen with $\alpha = 30°, \beta = 30°$; **c** fluid domain of double flaws specimen

Table 1 Geometric data for all specimens

	Flaw length (a)	Bridging length (b)	Flaw inclination angles (α)	Bridging angle (β)
Single flaw	3 mm	–	0°, 30°, 45°, 60°, 90°	–
Double flaws	3 mm	3 mm	30°	−60°, −30°, 0°, 30°, 60°, 90°, 120°

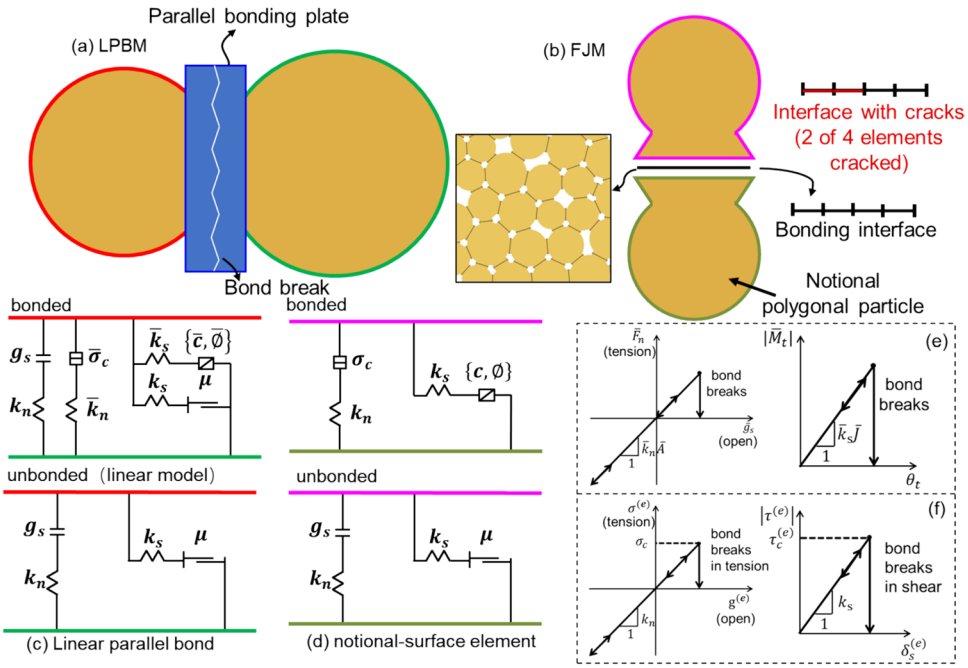

Fig. 5 Particle contact model used in HGTM. **a** schematic of LPBM (grain boundary); **b** schematic of FJM (intra-grain); **c** behavior and rheological components of LPBM; **d** behavior and rheological components of the FJM; force–displacement law for the **e** parallel bond and **f** FJM element

Employing FJM for IG contacts mitigates the tendency of LPBMs to overestimate breakdown pressures of hydraulic fracturing. The FJM has successfully simulated various rock types, such as granite, marble, tuff, limestone, and sandstone (Vallejos et al. 2017; Bai et al. 2022; Wu and Xu 2016; Chen 2017; Cheng and Wong 2020; Bahaaddini et al. 2021). The elastic, plastic, and failure responses exhibited by mineral grains correspondingly manifest as deformation, dislocations, and fractures. The presence of rotational moments in the LPBM leads to a significantly reduced ratio between uniaxial compressive strength and tensile strength compared with experimental results. The FJM has demonstrated capability in addressing this limitation due to its inherent strengths. The mechanical actions at grain boundaries including opening, sliding, or rotation can be accurately replicated using the LPBM model. Additionally,

in accordance with the proposal by Li et al. (2018), who introduced a modified LPBM to more accurately simulate grain boundaries, we have adopted this refined approach to enhance the precision of our modeling. A more detailed description of FJM and LPBM can be found in the prior references.

The microscale parameters are iteratively adjusted until the simulated macroscale response closely aligns with that of the actual rock. The parameter calibration for the GTM model was discussed in detail in our previous studies (Zhao et al. 2021): firstly, the parameters of the four mineral grains were calibrated using trial-and-error process, and then the reduction coefficient of grain boundaries were calibrated until the macroscopic mechanical parameters were consistent with the experimental results. As shown in Fig. 6, the crack distributions and stress–strain curves of the GTM model under uniaxial compression test and tensile test are presented. The resulting macroscale mechanical properties, from both experiments (Zhuang et al. 2019) and numerical modeling, are detailed in Table 2. The macro-mechanical properties derived from the GTM are in close correspondence to those observed in the experiments, indicating high fidelity and reliability of the GTM in representing the response of the Pocheon granite. The specifically calibrated micro-mechanical properties are listed in Table 3.

The values and calibration of hydraulic parameters of the granite have been extensively described in previous studies (Kong et al. 2021; Li et al. 2022; Wang et al. 2023), in which the validity of parameters was verified through methods such as Darcy test and comparison with the analytical solution of Khristianovic–Geertsma–de Klerk (KGD) model. As the primary focus of this paper does not involve a discussion of parameters, we will directly adopt the parameters from these previous studies. The hydraulic parameters utilized in this study are presented in Table 3.

3 Results for Analyses with Single Flaw

We conduct hydraulic fracturing tests on numerical specimens with a single flaw at various inclination angles (0°, 30°, 45°, 60°, 90°), both under orthogonal confining stress (vertical: 6 MPa; horizontal: 1 MPa) and without confining stress (vertical: 0 MPa; horizontal: 0 MPa). The influence of flaw inclination angles, mineral heterogeneity, and confining stress on the propagation of fluid-driven fractures during the hydraulic fracturing process was systematically investigated.

Table 2 Macroscale properties recovered from both experiment (Zhuang et al. 2019) and numerical simulation

Macroscale properties	Experiment	GTM
Uniaxial compressive strength, *UCS* (MPa)	174.1–215.1	193.9
Tension strength, *TS* (MPa)	6.1–8.8	7.8
Young's modulus, *E* (GPa)	54.5–59.1	54.1
Poisson's ratio, *ν*	0.25–0.31	0.25

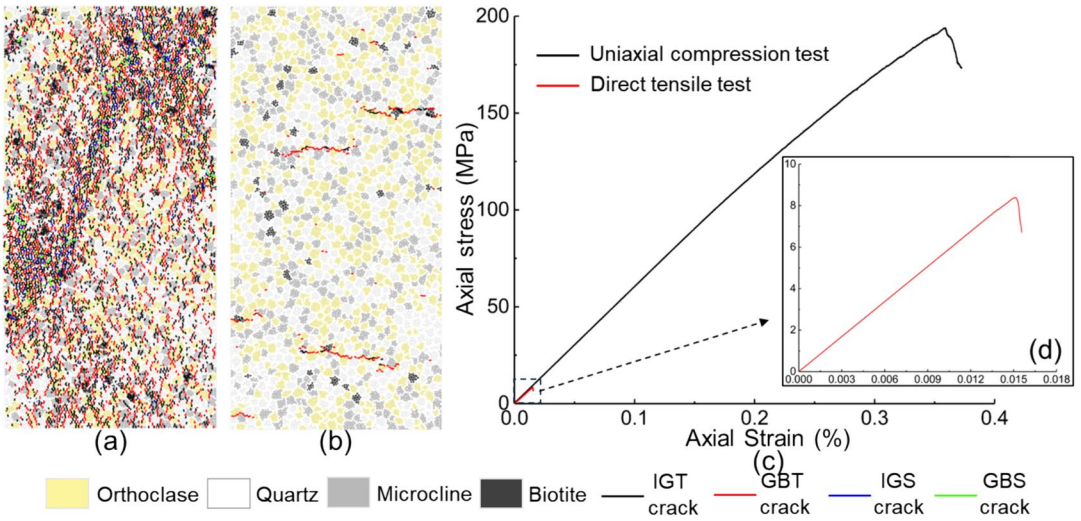

Fig. 6 GTM numerical test results: crack distributions under **a** uniaxial compression test and **b** direct tensile test; **c** axial stress–strain curves. *IGT* intra-grain tensile, *GBT* grain boundary tensile,*IGS* intra-grain shear, *GBS* grain boundary shear

Table 3 Microscale parameters representing the numerical specimen

Microscale parameters	Value			
	Orthoclase	Quartz	Microcline	Biotite
Micro-properties of particles and IG contacts (FJM)				
Mineral grain sizes, D (mm)	0.7–1.3	0.7–1.3	0.7–1.3	0.7–1.3
Mineral volume fractions	35.8%	35.8%	25.8%	2.6%
Sub- particle radii, r_{min} (mm)	0.1	0.1	0.1	0.1
Sub-grain size ratios, r_{max}/r_{min}	1.66	1.66	1.66	1.66
Densities, ρ(kg/m^3)	2560	2648	2670	3090
Contact effective moduli, E_c (GPa)	31.7	33.6	32.7	17.2
Tensile strengths, σ_t(MPa)	28.3	33.2	30.5	23.5
Bond cohesions, C (MPa)	195.0	292.0	198.9	95.0
Bond friction coefficients, μ (−)	0.5	0.5	0.5	0.5
Stiffness ratios, K_n/K_s	1.6	1	1.6	2.0
Bond friction angles, φ (◦)	35	45	35	35
Number of elements, Ne	4	4	4	4
Micro-properties of GB contacts (LPBM)				
Modulus reduction coefficient,α_E	0.6			
Stiffness ratio reduction coefficient,α_k	1			
Tensile strength reduction coefficient,α_t	0.5			
Cohesion reduction coefficient,α_c	0.5			
Friction coefficient reduction coefficient,α_μ	0.8			
Friction angle reduction coefficient,α_φ	0.9			
Hydraulic properties				
Initial aperture, w_{ini}(m)	1e^{-8}			
Fluid viscosity (mPa·s)	1			
Fluid bulk modulus (GPa)	2			
F_{ini}(N)	5.0e^7			
Aperture multiplier, d	0.5			
Injection rate (m^2/s)	1e^{-4}			
Flow time step, Δt_{flow} (s)	5e^{-6}			

3.1 Fracture Distribution

The evolution of hydraulic fractures is jointly determined by the confining stress conditions, mineral heterogeneities, and the flaw inclination angles (α), as presented in Fig. 7. Generally, with an increase in α, the differences in fracture morphologies under the two confining stress conditions decrease. The largest discrepancies are observed when $\alpha = 0°$, while they become minimal when $\alpha = 90°$. This phenomenon can be attributed to how confining stress influences the orientation of hydraulic fracture propagation.

When the confining stress is absent (0–0 MPa), hydraulic fractures propagate in various directions for different inclinations (α). Since to fracture initiation occurs along the long axis of the flaw, overall propagation initially continues in this particular orientation from the fracture tip. Nevertheless, during propagation, primary fractures extend preferentially along paths with lower strength: as grain boundaries possess low strengths, they exert a significant influence on fracture propagation. It is easier for the primary fracture to be captured by, and extend along, the grain boundaries. For instance, in the locally magnified image ($\alpha = 45°$) (Fig. 7c), fracture branches are formed between the mineral grain boundaries.

Where confining stress (6–1 MPa) is applied, fracture propagation is primarily influenced by the confining stress and extends toward the maximum principal stress. The fracture initiation process encompasses two distinct patterns, with the first pattern characterized by fractures predominantly propagating along the long axis of the pre-existing flaws during both initiation and initial stages of propagation. As propagation progresses, fractures begin to alter their orientations under the combined influence of grain boundaries and confining stress. For example, for $\alpha = 0°$, the primary fracture on the right side undergoes an approximately 90° change in its propagation orientation along a grain boundary, transitioning from horizontal to vertical (Fig. 7a). The second pattern of fracture initiation is directed vertically, exemplified by the primary fracture on the left side in the case of $\alpha = 30°/45°/60°$. This pattern is similar to that of a tensile

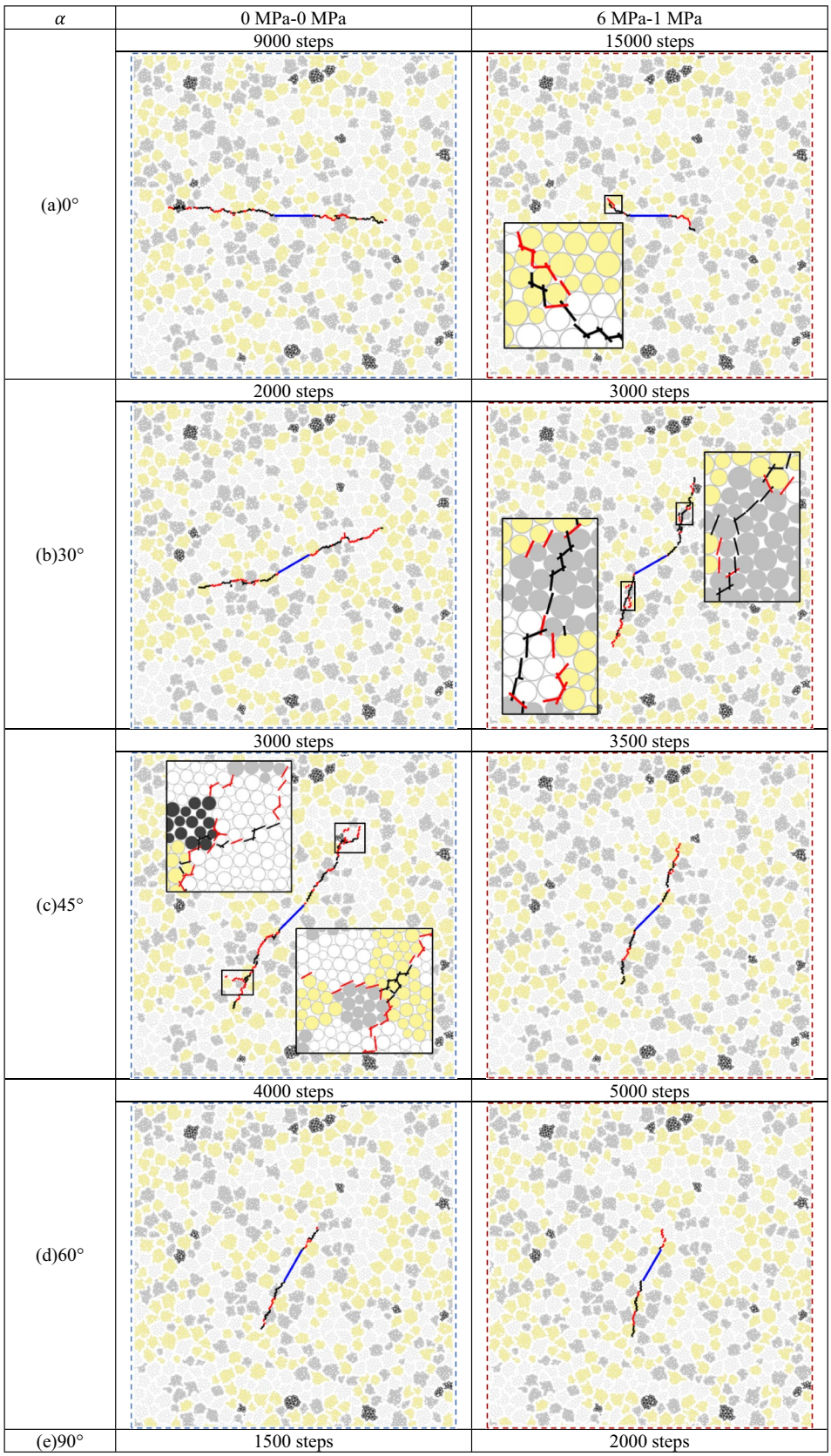

Fig. 7 Fluid-driven fracture distribution for a single flaw specimen with different inclination angles (α). *IG* intra-grain, *GB* grain boundary

Fig. 7 (continued)

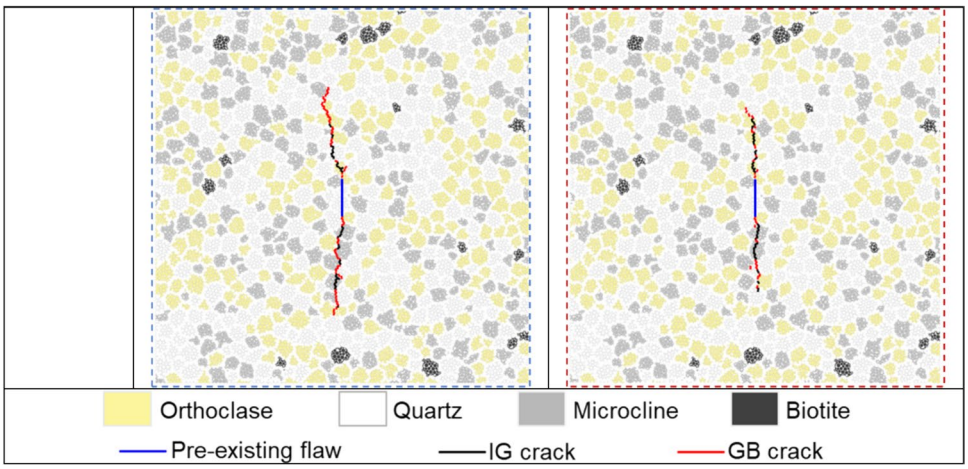

wing fracture in uniaxial compression (Fig. 1). Although the strength of the grain boundary is low, IG fracturing is still the main feature in hydraulic fracturing. Close-up views in Fig. 7a, b reveal isolated particles that mimic rock fragments near grain boundaries. Rock fragments like these are formed due to the interactions among hydraulic fractures and grain boundaries. This implies that when there is a notable difference in strength between mineral grains and grain boundaries, it tends to result in more complicated fracture propagation behavior.

3.2 Number of Cracks, Crack Orientation, and Fracture Tortuosity

Figure 8 shows the number of cracks and crack orientation results for the single flaw specimen under different α. In all cases discussed in this section, GB crack proportions ranged from 11.5% to 30.9%. The reason of IG cracks over GB cracks during hydraulic fracturing process is not attributed to the lower strength of the intra-grain compared to the grain boundary. Instead, it is associated with the orientation of hydraulic fracture incidence relative to mineral grains. A large incidence angle tends to result in IG fractures by crossing through grain boundaries, whereas a small angle increases the possibility of capturing the fracture at the grain boundary and producing GB fractures.

In contrast, simulations employing the GBM for mineral structural analysis often present unrealistic results, where the proportion of GB cracks are excessively high—surpassing 50% in certain cases (Li et al. 2022; Wang et al. 2023). This discrepancy stems from the requirement of the GBM for significantly reduced IG contact strength to simulate the high uniaxial compressive to tension strength ratio of granites. Conversely, our HGTM, incorporating intra-granular FJM and LPBM at grain boundaries, accurately reflects the proportion of GB cracks across the spectrum of conditions.

In the case of $\alpha = 0°$, the total number of cracks that develop in the absence of confining stress is significantly higher than that with confining stress (6–1 MPa)—due to fracture initiation predominantly occurring in the horizontal direction. The presence of a differential confining stress (strongly) favors propagation in the (vertical) direction of the maximum stress, making fracture propagation more complex compared to cases without confining stress. For α =60°/90°, the total number of cracks in the two confining stress conditions is almost equal, which is also related to the orientation of propagation of the fractures, which all extend in the vertical orientation after the fracture initiation.

Rose diagrams show the orientations of the various IG and GB cracks. The crack dip angle is defined as the angle measured counterclockwise from the negative x-direction to the microfracture orientation. The crack orientation exhibits a wide range of orientations. While the primary fracture demonstrates a distinct orientation, the angle of the cracks at microscopic scales diverges. This implies that different segments of the hydraulic fractures exhibit divergence in direction, consistent with the observations of tortuosity for hydraulic fractures in granite as confirmed by experimental studies (Li and Einstein 2019). Under a confining stress regime of 6–1 MPa, cracks oriented toward 90° still exist at $\alpha = 0°$, whereas no cracks at small-angle orientation are apparent at $\alpha = 60°/90°$.

The fracture tortuosity results for single flaw specimens are presented in Fig. 9 for various confining stress and flaw orientations. The tortuosity of the primary fractures was evaluated by calculating the ratio between the total length of the main fracture and the linear distance between its termini. Noticeable disparities in tortuosity are observed between the two different confining stress conditions. For the 0–0 MPa condition, the fracture propagation orientation extends along the orientation of initiation, the variation in tortuosity under different flaw inclination angle conditions is not significant. However, due to the existence

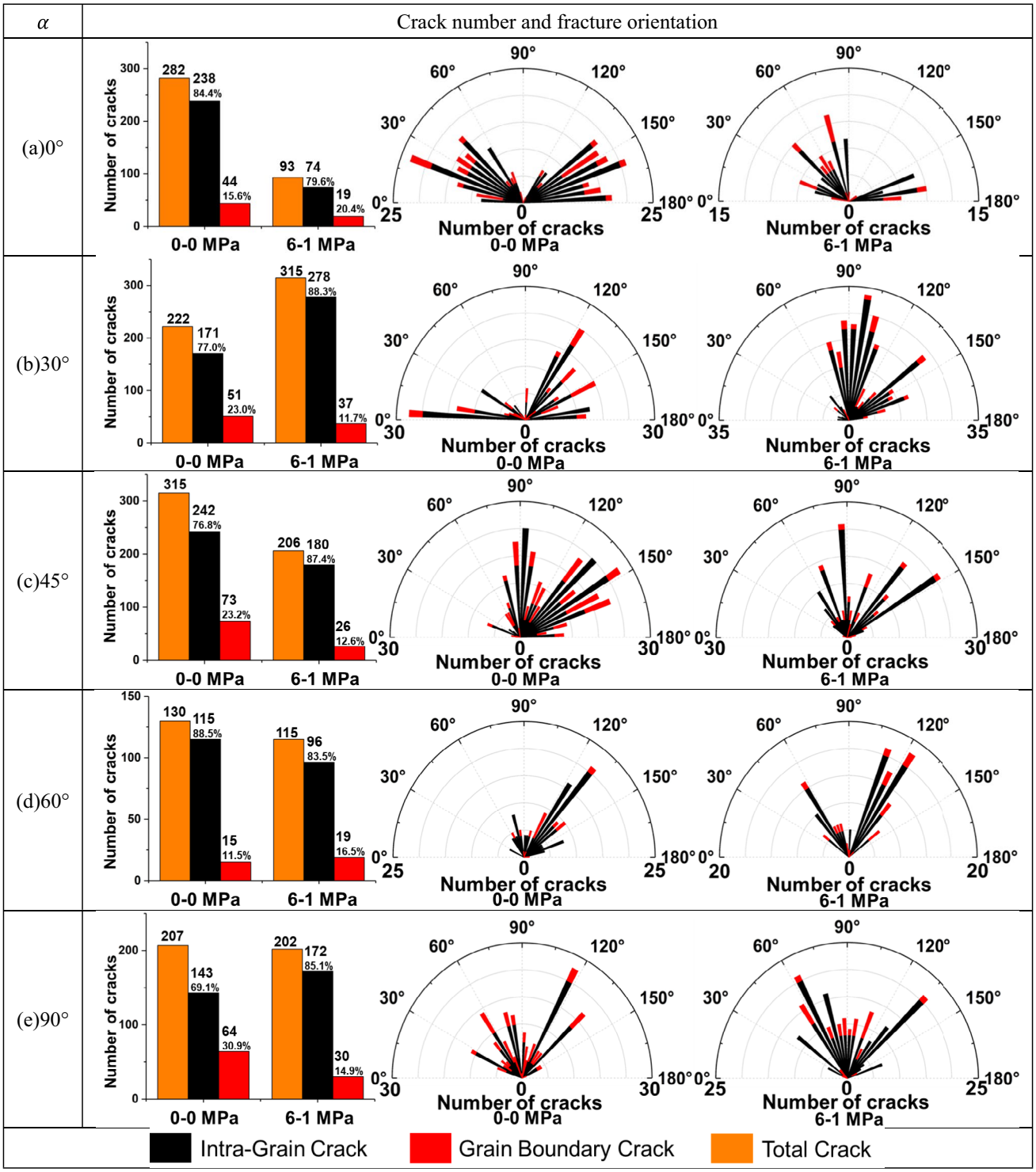

Fig. 8 Number of cracks and crack orientation statistics for a single flaw at different inclinations (α)

of mineral grain heterogeneity, the path of hydraulic fractures in different flaw inclination angle conditions encounters different mineral grains and mineral shapes, which also leads to slight differences in tortuosity. Conversely, for the 6–1 MPa condition, fractures extend vertically (in the direction of the 6 MPa stress), leading to a gradual reduction in tortuosity with increasing α. Specifically, for $\alpha = 0°$, where fracture initiation occurs horizontally and reorients vertically, the maximum tortuosity reaches 1.162.

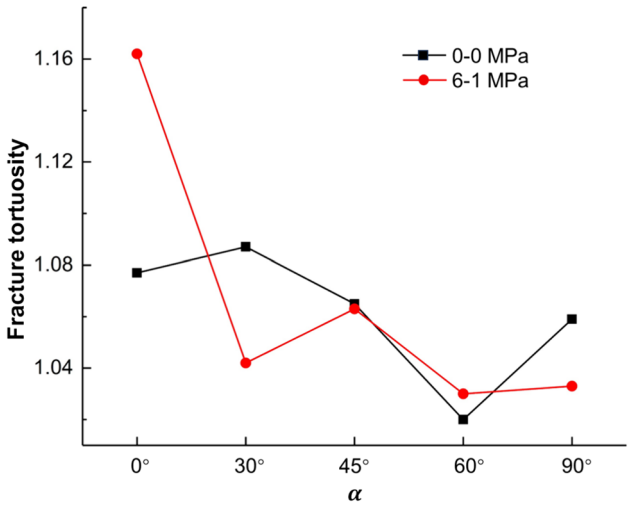

Fig. 9 Fracture tortuosity for rock specimens with single flaw at different inclinations (α)

4 Results for Analyses with Double Flaws

We also conduct hydraulic fracturing tests on numerical specimens containing double flaws at various bridging angles (−60°, −30°, 0°, 30°, 60°, 90°, 120°), both under confining stress (vertical: 6 MPa; horizontal: 1 MPa) and unstressed. The influence of flaw geometry, mineral heterogeneity, and confining stress on the propagation and coalescence of fluid-driven fractures during the hydraulic fracturing process was investigated.

4.1 Fracture Distribution

The hydraulic fracture distributions results for double flaw specimens with different bridging angles (β) but the same flaw inclination angle ($\alpha = 30°$) under the two stresses conditions are presented in Fig. 10. Both the β and confining stress conditions have an effect on the propagation and coalescence process of the fractures. Compared to the single flaw specimens, the fracture propagation for the double flaws is more intricate. Similar to single flaw specimens, fractures initiate from the tip of the flaw; however, their propagation is influenced by the other flaw, causing the inboard (in the center) primary fracture to extend in that direction. Additionally, confining stress also affects fracture propagation behavior. Under the absence of confining stress, the outboard (close to the specimen edges) primary fracture extends at 30° (flaw inclination angle), whereas under a confining stress condition of 6–1 MPa, fractures propagate vertically due to the overriding influence of the differential stress.

Fracture coalescence is significantly influenced by different bridging angles (β) and confining stresses. Based on the resulting fracture distributions, under no confining stress (0–0 MPa), fracture coalescence occurs for $\beta = -30°/0°/30°$, whereas under stressed (6–1 MPa), fracture coalescence occurs at $\beta = 30°/60°$. For a bridging angle of −60°, the inboard primary fracture of the right flaw exhibits fracture branching with one branch extending toward the other flaw and the other branch extending vertically (6–1 MPa). This phenomenon arises due to low strength of the grain boundaries causing vertical fracturing at the grain boundaries and forming fracture branches. When $\beta = 90°/120°$, similar propagation patterns of inboard primary fracture tip are observed under both confining stress conditions.

Experimental results for hydraulic fracturing in granite containing double flaws are presented in Fig. 11 (Goncalves and Einstein 2018). Two confining stress conditions similar to those in our numerical tests were considered: 0–0 MPa and a uniaxial vertical load of 5 MPa (5–0 MPa). Both the β and confining stress conditions affect the fracture coalescence patterns. Comparing the numerical results with the experimental results, it is evident that HGTM effectively reproduces the test outcomes of the hydraulic fracturing. The fracture coalescence patterns match well, coalescence occurring under experimental conditions of $\beta = 0°/30°$ (0–0 MPa), as well as $\beta = 30°/60°$ (5–0 MPa). Under conditions of $\beta = 90°/120°$, the influence of confining stress on fracture propagation patterns is minimal, which is also similar with our HGTM results. The influence of confining stress conditions on the propagation orientation of the outboard primary fracture is also in accordance with the principle of HGTM.

4.2 Fluid Pressure and Force Field

The distribution of fluid pressure field is illustrated in Fig. 12 for three different bridge angles ($\beta = -30°/30°/90°$) and our two different confining stress conditions. Due to the low permeability of granite, fluid pressure is localized within the hydraulic fractures with minimal flow into the rock matrix. In terms of the inboard primary fractures of the two flaws, their fluid pressure distribution aligns closely with the distribution of the hydraulic fractures; however, in the outboard primary fractures, the development of fluid pressure occurs over a shorter distance compared to the propagation of the hydraulic fractures. This is also known as the "dry fracture" effect. Garagash and Detournay (2000) elucidate this phenomenon by employing linear elasticity theory and assuming homogeneity of the material. As depicted in the three locally enlarged panels in Fig. 12, when hydraulic fractures coalesce, there is also coalescence in the high fluid pressure.

The distribution of horizontal and vertical fluid forces within the specimen is illustrated in Figs. 13 and 14, respectively. Upon injection into the fractured specimen, the fluid exerts pressure on the surrounding rock matrix, leading to a continuous extension of the hydraulic fracture. The force exerted by the fluid is applied local to the flaw and around

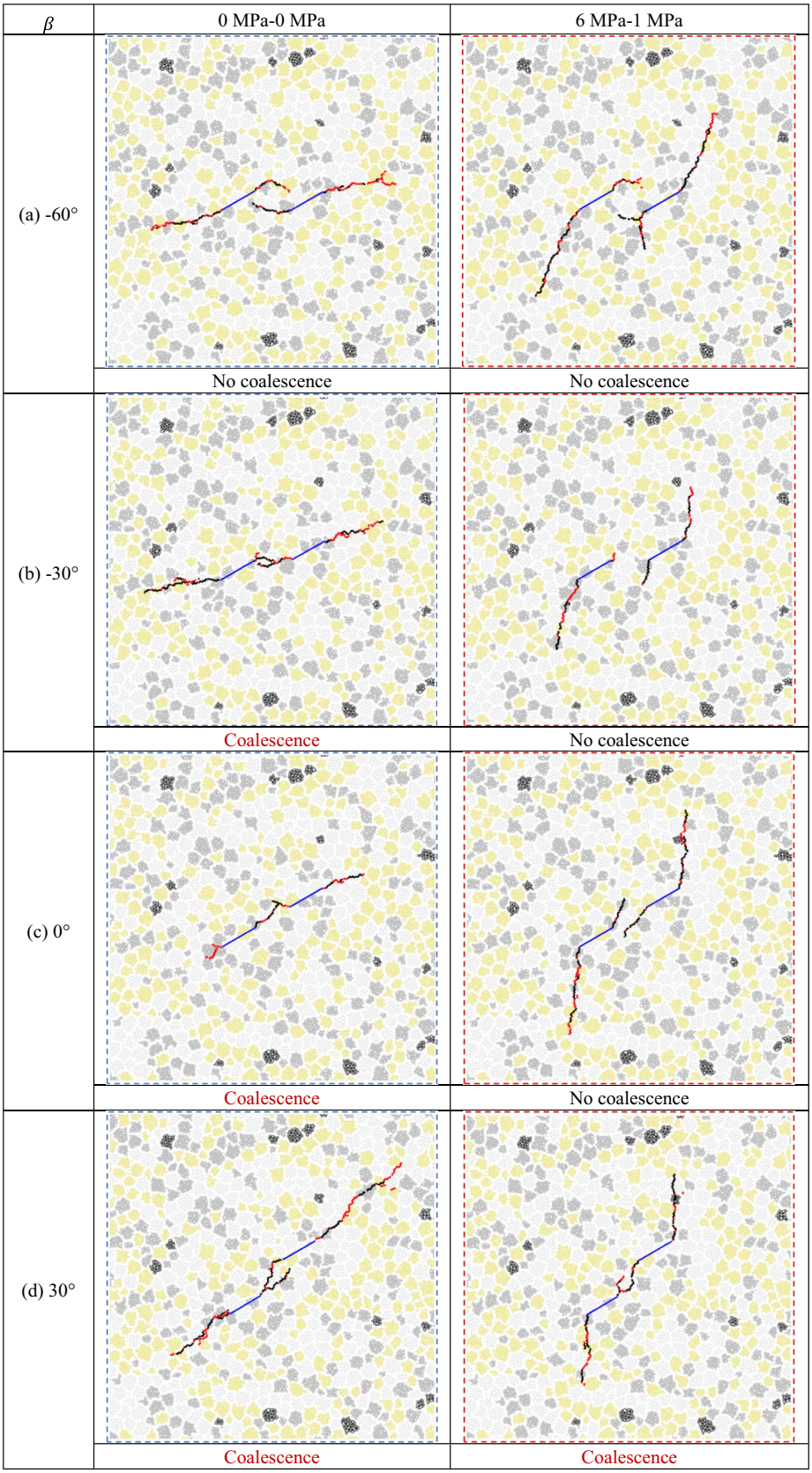

Fig. 10 Fluid-driven fracture distribution for double flaw specimens at different β ($\alpha = 30°$)

Fig. 10 (continued)

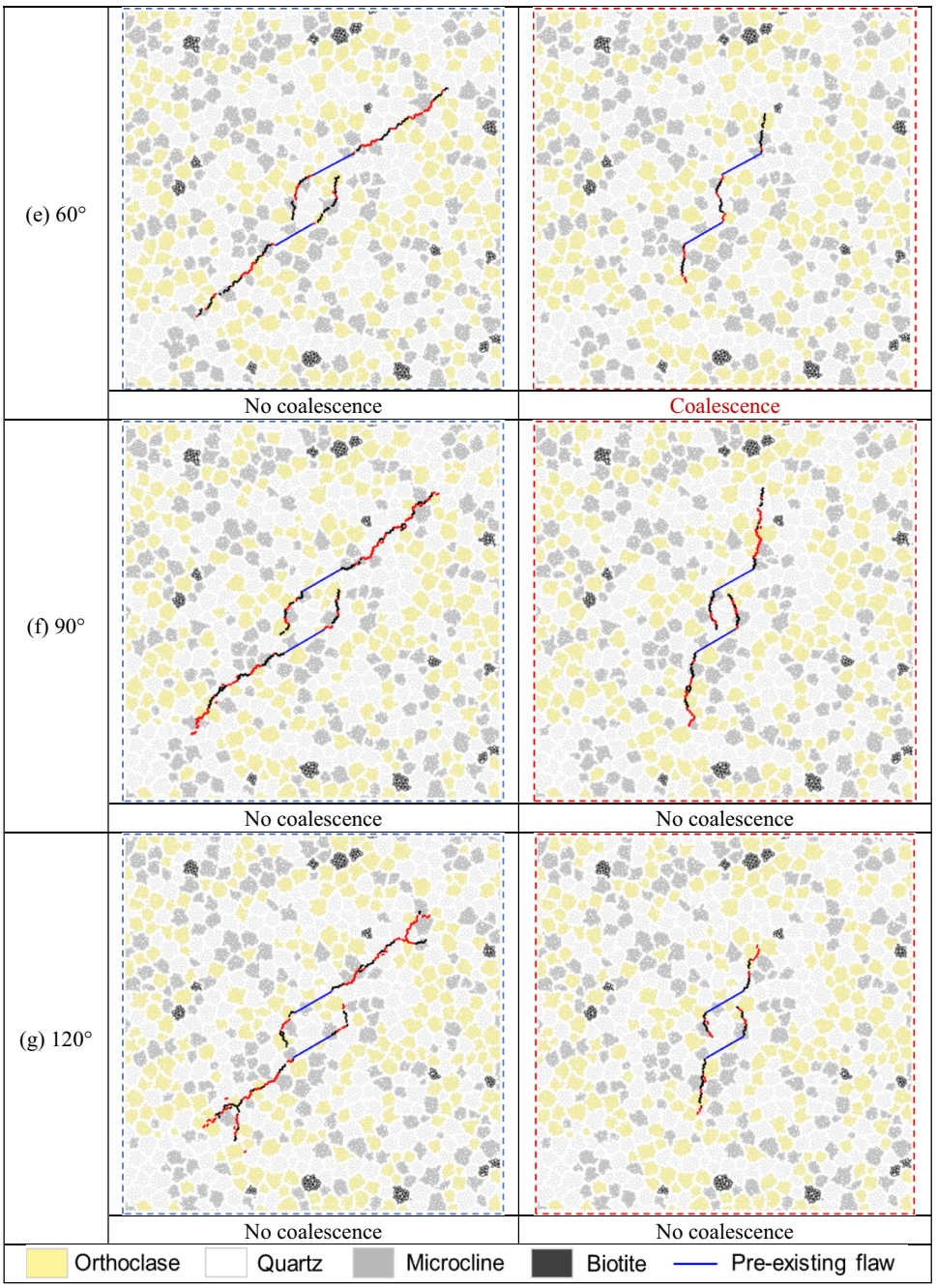

the pressurized hydraulic fractures. However, due to stress concentration at the tips of each flaw, initiation and propagation of the hydraulic fractures still occur predominantly at their respective tips.

For specimens stressed to 6–1 MPa, the fluid force in the outboard primary fracture is mainly horizontal, with a minimal vertical force. When the $\beta = -30°$ at 0–0 MPa, the hydraulic force in the outboard primary fracture is predominantly vertical—exactly opposite. As a result, the propagation direction of the outboard primary fracture is approximately horizontal, while the propagation direction of the outboard primary fracture at 6–1 MPa is approximately vertical. This phenomenon indicates that the fracture initiation pattern of hydraulic fracturing is significantly different from that under uniaxial compression—as expected. As shown in Fig. 15, the fracture under uniaxial compression propagates by horizontal tensile failure under a vertical compressive load. The initiation and propagation of fractures under hydraulic fracturing are due to tensile failure under the action of the fluid forces inside the fracture. Although both represent tensile failure, the cause is not the same. In addition, an interesting phenomenon was

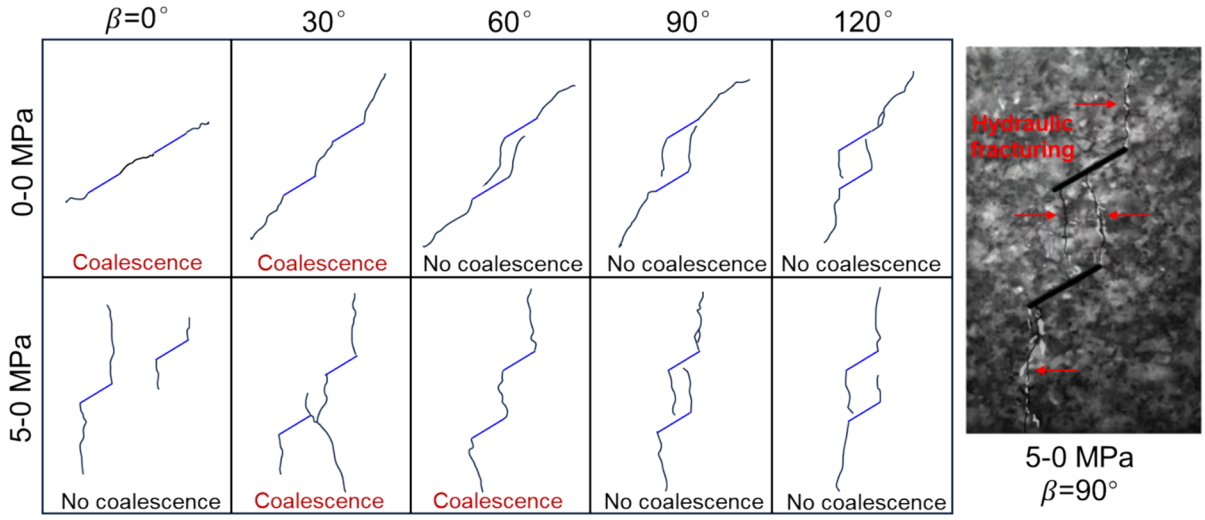

Fig. 11 Fluid-driven fracture distribution for different β ($\alpha = 30°$) (Gonçalves and Einstein 2018)

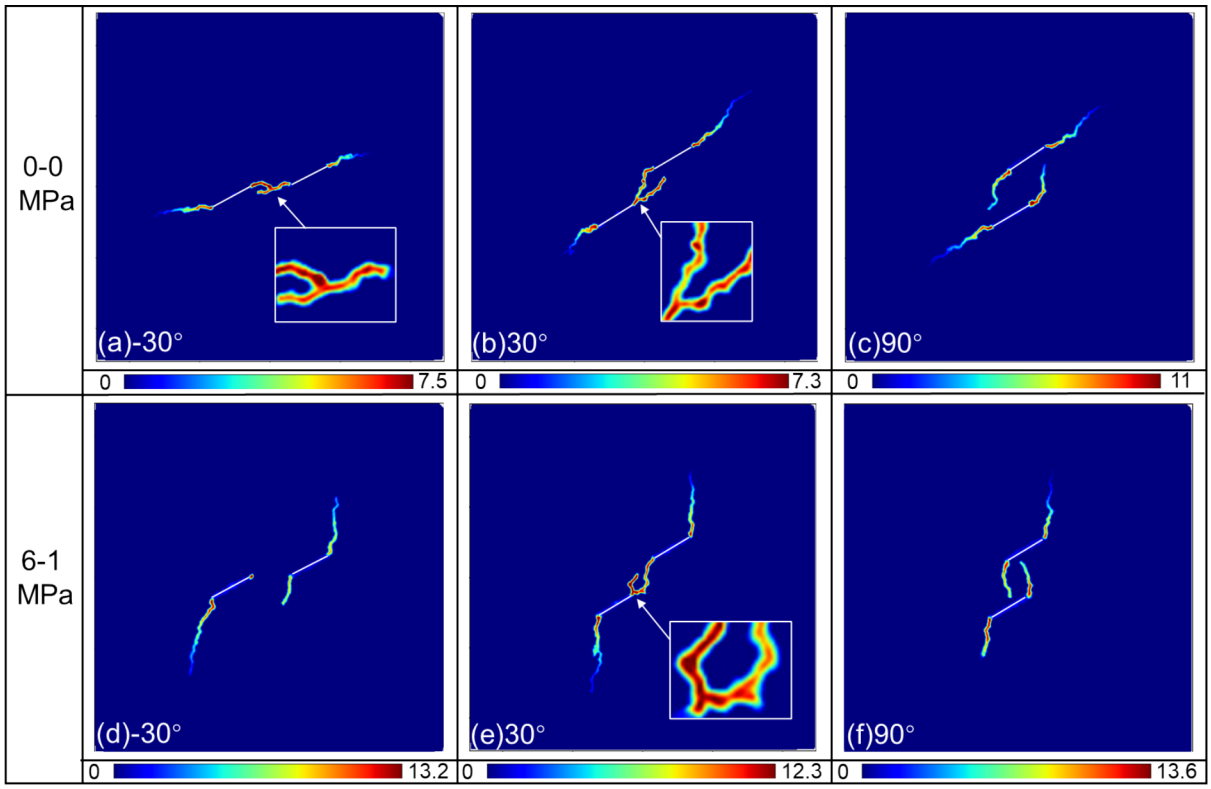

Fig. 12 Fluid pressure fields of double flaw specimen with $\beta = -30°/30°/90°$ (unit: MPa)

observed for $\beta = 30°$at 0–0 MPa, where the fluid force lagged far behind the extension of hydraulic fractures. In this case, although the fracturing fluid has not yet reached the tip of the fracture, the fracture still extends and creates a "dry region" representing the "lag" region where the fracturing fluid lags behind the propagation of the tip (Figs. 13b and 14b).

4.3 Displacement Field

The displacement field around the fracture is illustrated in Fig. 16, showing three different bridge angles

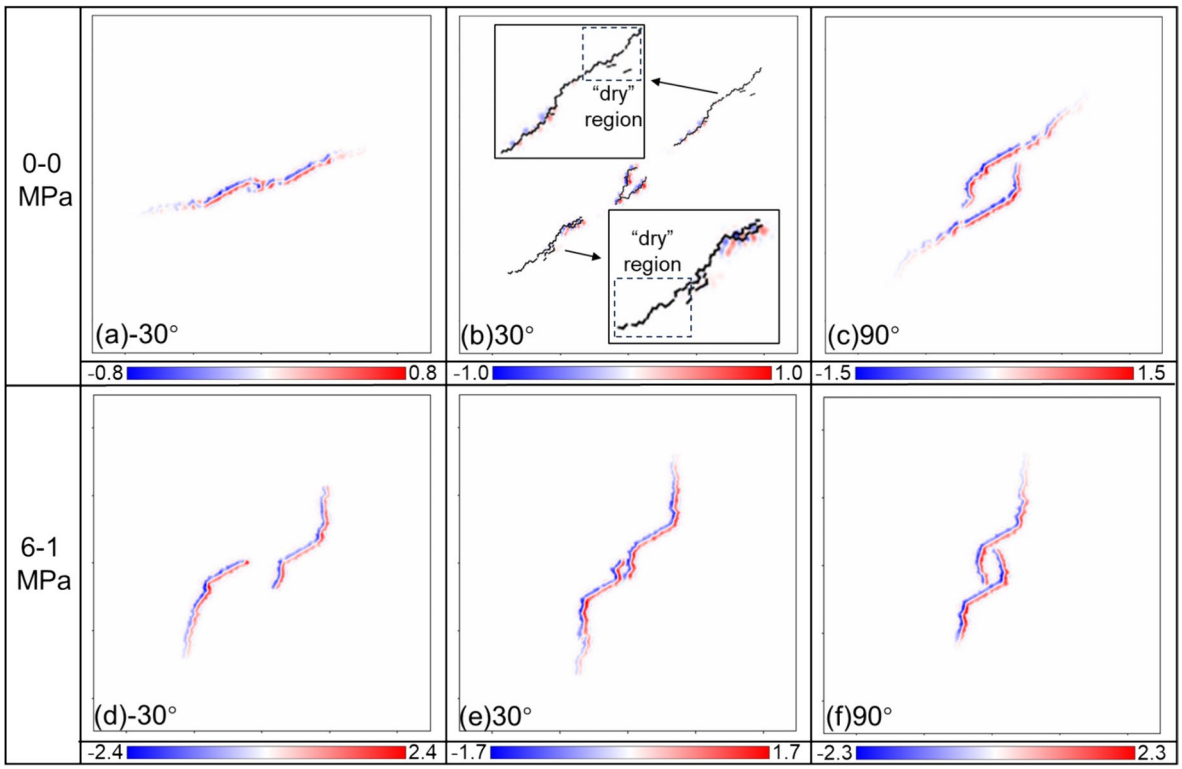

Fig. 13 Fluid force (horizontal-direction) fields for double flaw specimens under $\beta = -30°/30°/90°$ (unit: kN)

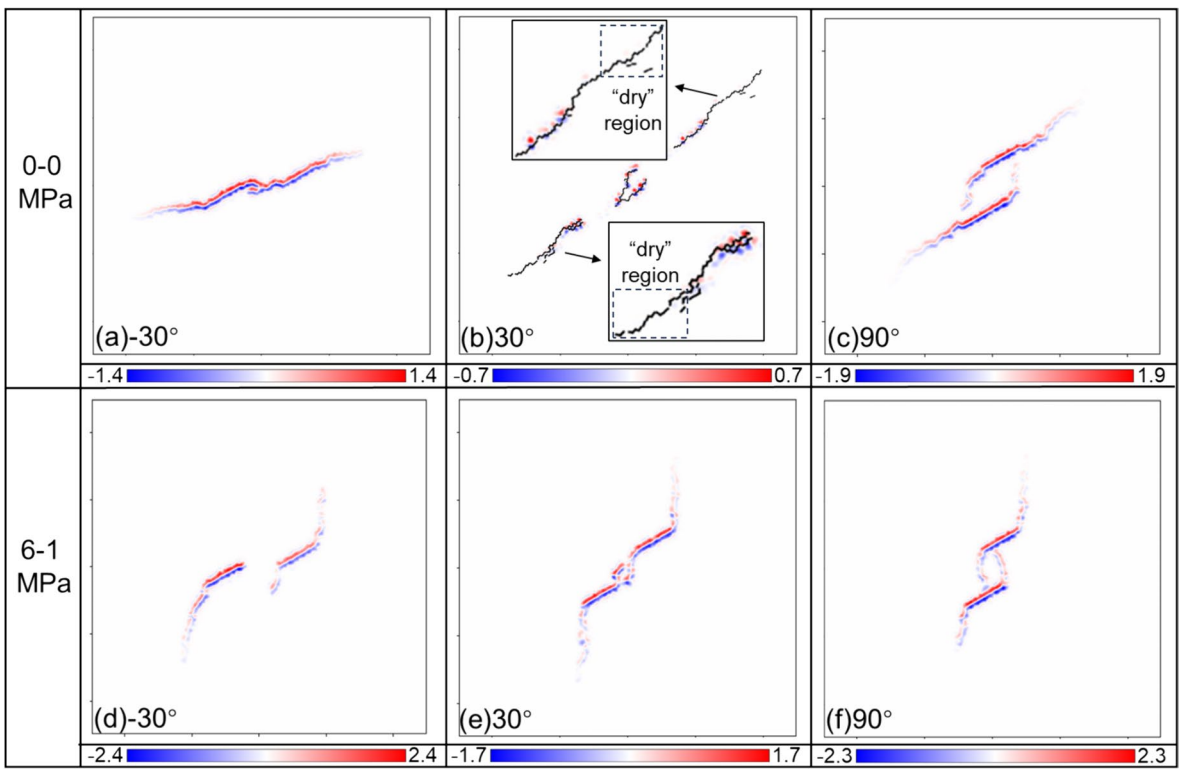

Fig. 14 Fluid force (vertical-direction) fields of double flaw specimens under $\beta = -30°/30°/90°$ (unit: kN)

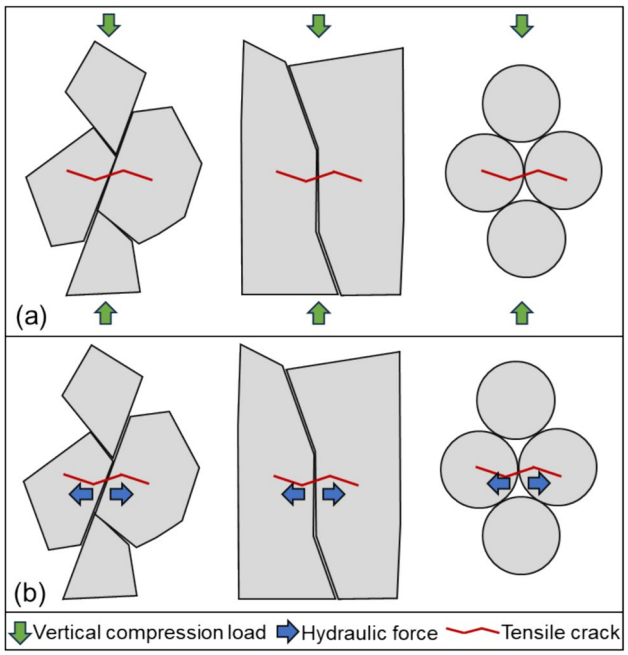

Fig. 15 Microstructural mechanisms in a cemented granular material that induce tensile fractures: **a** oriented perpendicular to the direction of compressive loading; **b** fluid force within a fracture

($\beta = -30°/30°/90°$) under our two confining stress conditions. The outboard primary fractures of the two flaws are in tension, segmenting the rock into two segments, as illustrated by the blue arrow in Fig. 16. However, the interaction between the inboard primary fractures introduces complexity to the displacement field between flaws. Under fracture coalescence, tensile displacement induces a slight rotational tendency in the displacement field between the flaws; at $\beta = 90°$, due to a stress shadow effect between the two inboard primary fractures, a clear rotational trend emerges in this displacement field opposite to the fracture propagation direction (red arrow in Fig. 16). This phenomenon further substantiates that pre-existing flaws exert significant influence on hydraulic fracture propagation and result in intricate fracture morphologies.

5 Breakdown Pressure

We may determine the effects of flaw geometry and confining stress on breakdown pressures. Figure 17 shows the evolution of crack number with injection pressure history for the double flaw specimen ($\alpha = 30°, \beta = 30°$). Due to the heterogeneity of the rock, the injection pressures in the two flaws are not exactly the same. As fracturing initiates, the fracturing fluid flows into the fracture, the injection pressure in the flaw begins to decrease and the maximum injection pressure represents the hydraulic fracturing breakdown pressure.

The breakdown pressures for the single flaw specimens with different α are presented in Fig. 18a. Under the same confining stress, α does not significantly or systematically impact breakdown pressure. At 0–0 MPa, the breakdown

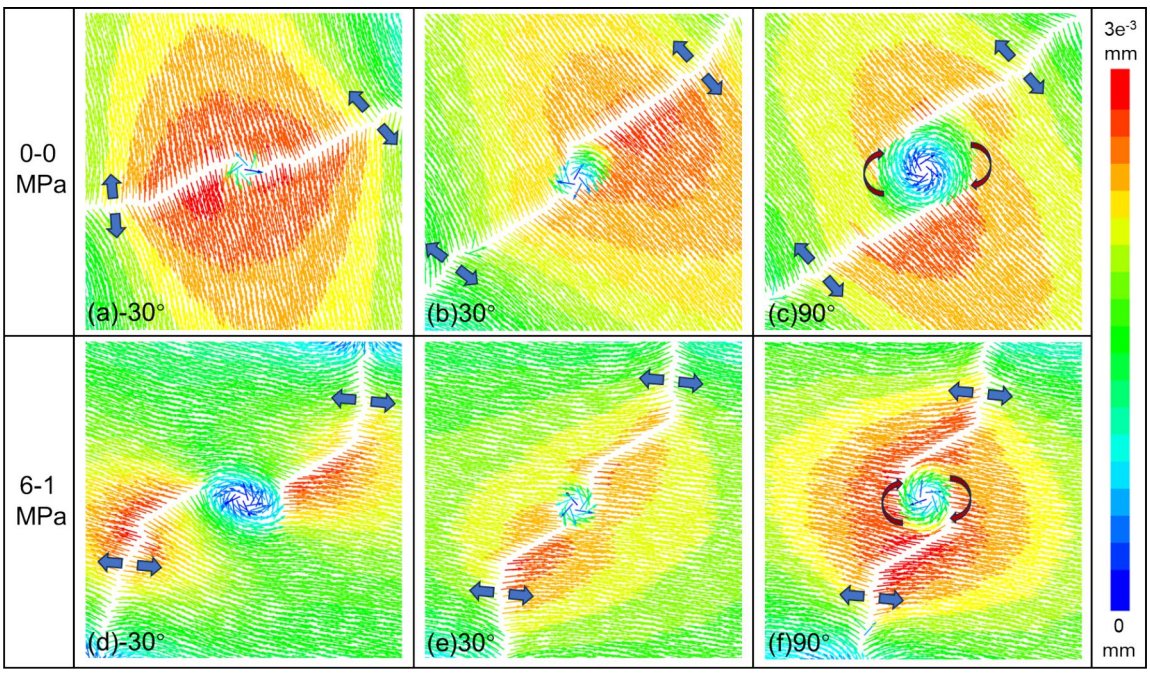

Fig. 16 Displacement fields for double flaw specimens under $\beta = -30°/30°/90°$ (15 mm * 15 mm)

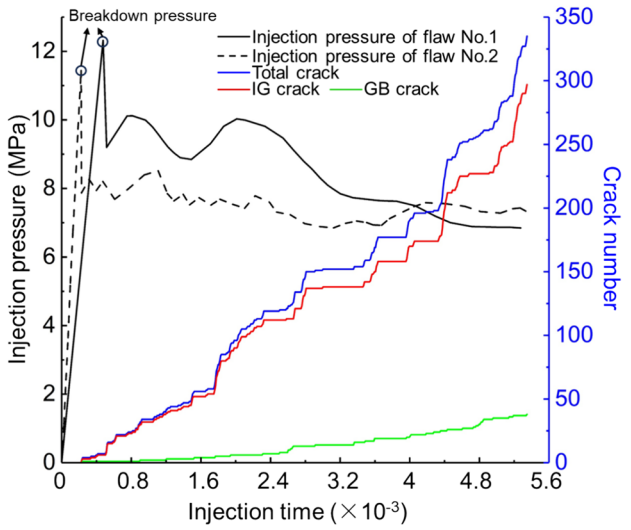

Fig. 17 Evolution of injection pressure and number of fractures with injection time for a double flaw specimen ($\alpha = 30°, \beta = 30°$). *IG* intra-grain, *GB* grain boundary

pressure ranges from 7.1 to 16.8 MPa—a factor of more than two. Mineral heterogeneity results in the varying breakdown pressures under different α. For instance, at $\alpha = 0°/60°$, a decrease in breakdown pressure is observed due to the presence of smaller local tensile strength at the flaw tip. The trend of breakdown pressures shows similarity with changes in α under both confining stresses; however, for a confining stress of 6–1 MPa, a higher breakdown pressure is obtained compared to that under 0–0 MPa conditions. This discrepancy is attributed to considering both the tensile strength and closure effect exerted by the confining stress on the flaw tip during hydraulic fracture initiation.

There is an apparently linear relationship between the difference in breakdown pressure and the α under the two confining stress conditions. As α increases, the difference in breakdown pressure gradually diminishes. When α reaches 90°, the difference in breakdown pressure under both stress conditions becomes small, which is consistent with the identical fracture distribution observed in Sect. 3.1. This outcome is attributed to variations in applied confining stress, specifically, confinement in the vertical direction of 6 MPa compared that in the horizontal direction of only 1 MPa. As shown in Fig. 18c, under the condition of 6–1 MPa confining stress and $\alpha = 0°$, the tip of the flaw generated a large local compressive stress after being subjected to vertical load. In cases involving low α, fracture initiation necessitates overcoming higher closure stresses; conversely, high α requires overcoming lower closure stresses.

The breakdown pressures for the double flaw specimens with different β are presented in Fig. 18b. The breakdown pressures of specimens with β ranging from −30° to 90° exhibit less fluctuation under the same confining stress, whereas it significantly increases at −60° and 120°. The trend of breakdown pressure variation with β remains similar under both stress conditions; however, at 6–1 MPa, the breakdown pressure surpasses that at 0–0 MPa, consistent with the results obtained for single flaw specimens. The pressure difference between the two confining stresses tends to decrease as β increases; nevertheless, within the range 0°–60°, the pressure difference remains relatively constant.

In summary, the breakdown pressures for both single and double flaw specimens is determined by the interplay between flaw geometry, confining stress conditions and mineral heterogeneity.

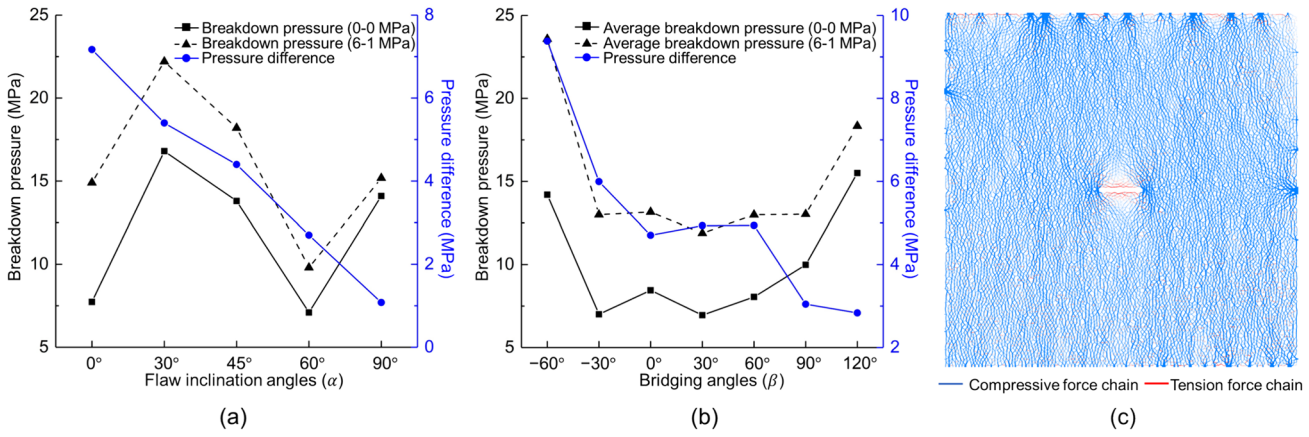

Fig. 18 Breakdown pressure and breakdown pressure difference for specimens under two contrasting confining stress conditions: **a** single flaw; **b** double flaws; **c** force chain distribution (6–1 MPa $\alpha = 0°$;)

6 Discussion

Fluid-driven fracture distributions of granite under the uniform and high obliquity confining stress conditions when the bridging angle is 30° are illustrated in Fig. 19a–h (Gunarathna and Gonçalves 2019). Under hydrostatic confining stress, GB fractures dominate, while under non-hydrostatic confining stress, IG fractures dominate. In Fig. 19i, the hydraulic fracturing results demonstrate the significant influence of mica on the hydraulic fracturing behavior, with hydraulic fractures consistently propagating along the mica boundaries (Zhuang and Zang 2021).

The percentage of GB fractures under the two confining stresses and for different bridging angles in the HGTM is presented in Table 4. The proportion of GB fractures is comparatively reduced at elevated confining stresses (6–1 MPa), as compared to that observed at null stress (0–0 MPa). This is because without the influence of confining stress, fracture propagation tends to extend toward the grain boundary with lower strength. Driven by confining stress, the fracture propagation has a specific direction. If 0–0 MPa is regarded as the hydrostatic stress condition, it can be found that the numerical results and the experimental results exhibit a discrepancy. This discrepancy with experimental results can be attributed to the mineral heterogeneity present, which often results in distinctly different results even when tests are conducted on the same type of granite. In addition, confining stress states may also be the key factor causing this difference. Future efforts should focus on further improvements and extensions of the HGTM, including three-dimensional models that consider the effects of intermediate stress and the very specific characteristics of the micas.

Table 4 Proportion of GB fractures in numerical double flaw specimens

Bridging Angle (β)	0–0 MPa	6–1 MPa	Difference value
−60°	0.247	0.124	+0.123
−30°	0.134	0.126	+0.008
0°	0.213	0.129	+0.084
30°	0.162	0.125	+0.037
60°	0.153	0.128	+0.025
90°	0.199	0.195	+0.004
120°	0.256	0.133	+0.123

7 Conclusions

Particle discrete element model of granites containing pre-existing flaws has been utilized to investigate the contrasting macro-mechanical responses resulting from microfracture evolution. These have included the influence of various loading conditions and the orientations of pre-existing flaws. We propose a hydro-grain-texture model (HGTM) based on a "grain growth" algorithm and fluid-domain-pipe model (FDPM) to accurately characterize the microstructure of granites subjected to hydraulic fracturing. By introducing single and double flaws in different orientations and relative to each other, we explore mechanisms controlling hydraulic fracturing in granites under the combined influence of

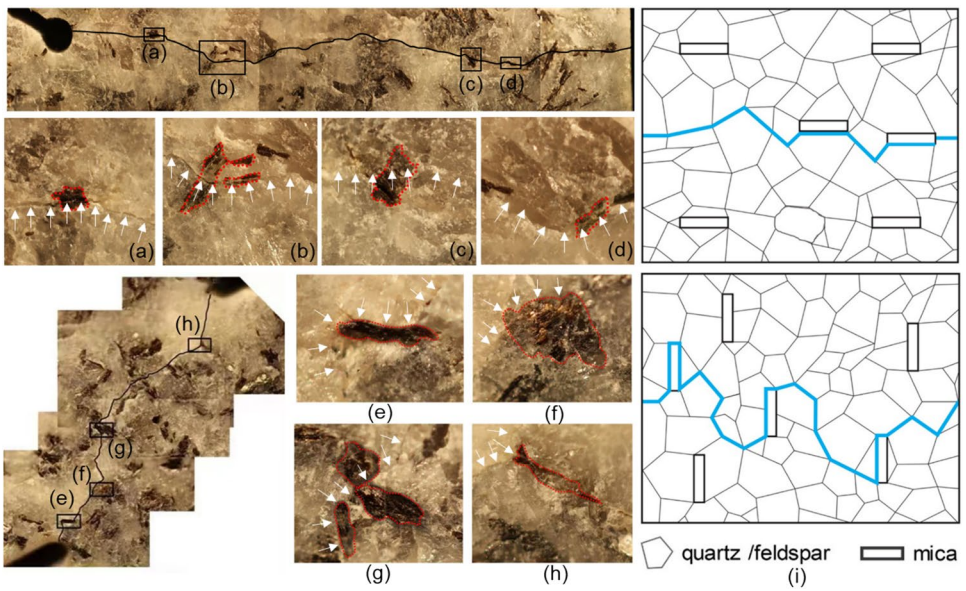

Fig. 19 Fluid-driven fracture distributions in experiments ($\beta = 30°$) under optical magnification: **a–d** the predominance of IG fractures under 2:2:2 MPa (vertical:lateral:out-of-plane); **e–h** predominance of GB fractures under 4:2:2 MPa (Gunarathna and Gonçalves 2019); **i** fluid-driven fracture distributions in granite. Maximum stress orientation is aligned parallel and perpendicular to the foliation. Blue indicates the path of the hydraulic fracture (Zhuang and Zang 2021)

mineral heterogeneity, confining stresses, and flaw geometries. The following conclusions are drawn:

(1) HGTM incorporating prefabricated flaws effectively captures the complex process of fluid-driven fracture initiation, propagation, and coalescence. From a microscopic perspective, HGTM comprehensively considers the influence of mineralogical heterogeneity and physical property anisotropy on hydraulic fracturing. The numerical modeling results are in good agreement with the experimental results in all cases.

(2) Absent confining stresses, the hydraulic fracture initiates at the tip of the flaw and predominantly expands in the direction of the long axis of the flaw. During propagation, extension is also influenced by transected weak grain boundaries, leading to secondary fractures and fracture branching phenomena. Under confining stress of high obliquity (6–1 MPa), regardless of flaw orientation and geometry, the hydraulic fractures consistently propagate toward the orientation of the maximum stress. These influencing factors result in broad variations in coalescence patterns, the number and type of fractures, as well as the resulting tortuosity of the hydraulic fractures.

(3) In all single flaw specimens, GB crack proportions ranged from 11.5% to 30.9%, closely mirroring physical experimental results which indicate return GB crack proportions between 0.3% and 30.3%. The angle of the cracks at microscopic scales can exhibit divergence. This implies that different segments of the hydraulic fractures exhibit divergence in direction, consistent with the observations of tortuosity for hydraulic fractures in granite as confirmed by experimental studies.

(4) In the low matrix permeability granite, fluid pressures are predominantly concentrated within the hydraulic fractures with minimal flow into the rock matrix. The fracturing fluid exerts pressure on the surrounding rock matrix, leading to continuous extension of the hydraulic fracture to accommodate the growing fluid volume. The primary fractures extending from the flaw tips are in tension, dividing the specimen into two segments. However, the cause of tensile failure under hydraulic fracturing and uniaxial compression test is different. In the case of uniaxial compression loading, horizontal tensile failure is induced by the vertical compression load, whereas in hydraulic fracturing, volume expansion occurs as a result of fluid pressure within the fractures.

(5) Breakdown pressures during hydraulic fracturing are influenced by the flaw geometry, confining stress conditions, and mineral heterogeneity. Without confining stress, the flaw geometry has minimal influence on breakdown pressure; instead, it is primarily determined by the local strength at the flaw tip. Breakdown pressure increases under confining stress (6–1 MPa) compared to the unstressed condition, and in the single flaw specimen, a linear relationship is established between breakdown pressure difference and flaw inclination angle (α).

Appendix A: Fluid-Domain-Pipe Model (FDPM)

Figure 3c illustrates a fluid pipe connecting two adjacent particles, conceptualized as a parallel plate similar to the LPBM depicted in Fig. 3a. The flow rate q between two neighboring domains is calculated using the Poiseuille equation:

$$q = \frac{w^3}{12\mu}\frac{\Delta p}{l}, \tag{1}$$

where w is the pipe aperture; μ is the fluid's viscosity; Δp is the fluid pressure difference between adjacent fluid domains; and l is the pipe length, which is assumed to the sum of the particle's radius: $l = r_1 + r_2$ (Fig. 3c).

The w keeps getting updated in response to the normal force acting on the pipe. A fluid pipe is deemed narrowed if the normal force is in compression. Conversely, if the normal force is in tension or the bonded contact breaks, the fluid pipe will open. The calculation of the aperture under these conditions proceeds as follows:

$$w = \begin{cases} \frac{w_{\text{ini}}F_{\text{ini}}}{F_{\text{ini}}+F}\,(\text{in compression}) \\ \\ w_{\text{ini}} + d\Delta w_{\text{gap}}(\text{in tension or broken}) \end{cases}, \tag{2}$$

where w_{ini} is the initial aperture; F is the pipe normal force; F_{ini} is the pipe normal force when the aperture value is reduced to half of w_{ini}; d is identified as the aperture multiplier; and Δw_{gap} is the variation in the contact gap between two particles.

The variation in fluid pressure Δp within a fluid domain can be determined by the fluid bulk modulus K_{fluid}, variation in fluid domain volume due to mechanical deformation ΔV_{domain} and the domain's volume V_{domain}:

$$\Delta p = K_{\text{fluid}}\left(\sum q\Delta t_{\text{flow}} - \Delta V_{\text{domain}}/V_{\text{domain}}\right), \tag{3}$$

where $\sum q$ is the total flow rate per flow time step in the domain and Δt_{flow} is the flow time step. The domain's pressure is updated every flow time step, applying force to the adjacent particles. These updated mechanical loads will affect the apertures of fluid pipes and domain volumes, thereby impacting subsequent flow calculations. When the

bonded contact breaks, the fluid flow is instantaneous, and that the fluid pressure in fluid domains is assumed to be their average value p_{fluid} before the bonded contact failure. The calculation of the new fluid pressure is given as

$$p_{\text{fluid}} = \frac{p_{\text{domain1}} + p_{\text{domain2}}}{2}. \tag{4}$$

In the coupled process of fluid flow and rock deformation, determining the fluid time step within each calculation step is crucial for maintaining numerical stability. Assuming the smallest pressure difference between a fluid domain and its adjacent fluid domain is Δp_{pmin}, it is possible to compute the total flow rate per step within the fluid domain:

$$\sum q \geq \Delta p_{\text{pmin}} \sum \frac{\omega^3}{(12\mu l)}. \tag{5}$$

Based on Eq. (3), the variation of fluid pressure Δp_c within a domain for each time step should not exceed the minimum pressure difference Δp_{pmin}, so that the direction of the pressure gradient remains unchanged: $\Delta p_c \leq \Delta p_{\text{pmin}}$. By integrating this principle with Eq. (3) and (5), the fluid time step necessary for ensuring calculation stability can be mathematically defined as

$$\Delta t_{\text{flow}} \leq \frac{\Delta V_{\text{domain}}}{\sum q} + \frac{V_{\text{domain}}}{K_{\text{fluid}} \sum \frac{\omega^3}{(12\mu l)}}. \tag{6}$$

More descriptions of this fluid flow model and its coupling with DEM in PFC can be found in our previous studies (Wang et al. 2014; 2017).

Appendix B: Linear Parallel Bond Model (LPBM)

LPBM, as one of the BPMs, is often used to simulate the crack initiation and propagation behavior of rocks under load. LPBM simulates the damage process of rocks by reducing the bonding area in a parallel form with linear elements (Fig. 5c), which is a fine-grained contact model that is highly consistent with fracture mechanics and damage mechanics. As shown in Fig. 5, the force–displacement law of LPBM is

$$F_c = F_l + F_p + F_d, M_c = M_p, \tag{7}$$

where F_c is the contact force; M_c is the moment; F_l is the linear force; F_p is the parallel-bond force; M_p is the parallel-bond moment; and F_d is the dashpot force. The linear element is co-displaced with the bonded element:

$$\begin{aligned} F_l &= -k_n \Delta\delta_n n + k_s \Delta\delta_s s, \\ F_p &= -\overline{k}_n \overline{A} \Delta\delta_n n + \overline{k}_s \overline{A} \Delta\delta_s s, \\ M_p &= \overline{M}_t n + \overline{M}_b, \end{aligned} \tag{8}$$

where k_n and k_s are the normal and tangential stiffness of linear elements, respectively; $\overline{k}_n$ and $\overline{k}_s$ are the normal and tangential stiffness per unit area of parallel bonded elements, respectively; $\overline{A}$ is bonding area; $\overline{M}_t$ and $\overline{M}_b$ are torsion moment and bending moment of parallel bond, respectively; $\Delta\delta_n$ and $\Delta\delta_s$ are the normal displacement and tangential displacement vectors of the contact, respectively; and n and s are the normal vector and tangential vector of the contact surface, respectively. The parallel-bond surface gap is defined as the cumulative relative normal displacement of the piece surfaces: $\overline{g}_s = \sum \Delta\delta_n$.

When LPBM is bonded, the stress on the parallel bonding element is

$$\begin{aligned} \overline{\sigma} &= \frac{\overline{F}_n}{\overline{A}} + \beta \frac{\|M_b\|}{\overline{I}}, \\ \overline{\tau} &= \frac{\overline{F}_S}{\overline{A}} + \beta \frac{|\overline{M}_t| R}{\overline{J}}, \\ \beta &\in [0, 1], \end{aligned} \tag{9}$$

where $\overline{F}_n$ and $\overline{F}_S$ are the normal force and shear force of parallel bonded elements, respectively; $\overline{I}$ and $\overline{J}$ are the moments of inertia and polarity of parallel bonded elements, respectively; β is the moment contribution coefficient.

If the tensile strength (σ_c) or shear strength ($\tau_c = c - \overline{\sigma} \tan \emptyset$, c is the cohesion and $\emptyset$ is the friction angle) is exceeded by normal stress ($\overline{\sigma}$) or shear stress ($\overline{\tau}$), then the bond will break in tensile or shear.

Appendix C: Flat-Joint Model (FJM)

The FJM divides the bonding interface into several elements, each of which can be damaged independently (Fig. 5). As the normal stress ($\sigma_n, \sigma_n > 0$ is in tensile),

$$\sigma_n = \begin{cases} 0, \text{unbonded and} g \geq 0 \\ k_n g \end{cases}, \tag{10}$$

where k_n is the normal stiffness and g is the particle gap. The σ_n is based on the gap, and the unbonded element with a positive gap carries no load. A tension load is carried only in a bonded element with a positive gap, and a compressive load is carried wherever the gap is negative, and when the normal stress exceeds the corresponding tensile strength (σ_c), the bond will break in tensile failure mode. The bond will break in shear failure mode when the shear stress exceeds the corresponding shear strength in a bonded element ($\tau = c - \sigma \tan \emptyset$, c is the cohesion, $\emptyset$ is the frictional

angle). Once the element is broken, it follows a slip envelope where only a shear stress ($\tau = -\mu\sigma$, μ is the friction coefficient) can be sustained.

Acknowledgements This work was supported by the program of China Scholarship Council (CSC No. 202306270120). DE gratefully acknowledges support from the G. Albert Shoemaker endowment.

Funding This work was supported by China Scholarship Council (No. 202306270120) and G. Albert Shoemaker endowment.

Data Availability Data will be made available on request.

Declarations

Conflict of Interest All the authors declared that there is no conflict of interest.

References

Adachi J, Siebrits E, Peirce A, Desroches J (2007) Computer simulation of hydraulic fractures. Int J Rock Mech Min Sci 44(1):739–757

Bahaaddini M, Sheikhpourkhani AM, Mansouri H (2021) Flat-joint model to reproduce the mechanical behaviour of intact rocks. Eur J Environ Civ Eng 25(8):1427–1448

Bai Q, Zhang C, Konietzky H, Young RP (2022) Simulation of seismic velocity changes in brittle rocks subjected to triaxial stresses using 3-D microstructural models. Geophys J Int 231(1):552–566

Bobet A, Einstein HH (1998) Fracture coalescence in rock-type materials under uniaxial and biaxial compression. Int J Rock Mech Min Sci 35(7):863–888

Chen P (2017) Effects of microparameters on macroparameters of flat-jointed bonded-particle materials and suggestions on trial-and-error method. Geotech Geol Eng 35(2):663–677. https://doi.org/10.1007/s10706-016-0132-5

Cheng Y, Wong LNY (2018) Microscopic characterization of tensile and shear fracturing in progressive failure in marble. J Geophys Res Solid Earth 123(1):204–225

Cheng Y, Wong LNY (2020) A study on mechanical properties and fracturing behavior of Carrara marble with the flat-joint model. Int J Numer Anal Met 44(6):803–822

Cheng H, Zhou X, Zhu J, Qian Q (2016) The effects of crack openings on crack initiation, propagation and coalescence behavior in rock-like materials under uniaxial compression. Rock Mech Rock Eng 49(9):3481–3494

Cho N, Martin CD, Sego DC (2007) A clumped particle model for rock. Int J Rock Mech Min 44(7):997–1010

Cundall PA, Strack OD (1979) A discrete numerical model for granular assemblies. Geotechnique 29(1):47–65

Garagash D, Detournay E (2000) The tip region of a fluid-driven fracture in an elastic medium. J Appl Mech 67(1):183–192

Gonçalves Da Silva B (2016) Fracturing processes and induced seismicity due to the hydraulic fracturing of rocks. Massachusetts Institute of Technology, Massachusetts (**PhD Thesis**)

Gonçalves Da Silva B, Einstein H (2018) Physical processes involved in the laboratory hydraulic fracturing of granite: visual observations and interpretation. Eng Fract Mech 191:125–142

Gunarathna G, Da Silva BG (2019) Influence of the effective vertical stresses on hydraulic fracture initiation pressures in shale and engineered geothermal systems explorations. Rock Mech Rock Eng 52(11):4835–4853

Gunarathna G, Gonçalves Da Silva B (2021) Effect of the triaxial state of stress in the hydraulic fracturing processes of granite: part 1—visual observations and interpretation. Rock Mech Rock Eng 54(6):2903–2923

Hofmann H, Babadagli T, Yoon JS et al (2015) A grain-based modeling study of mineralogical factors affecting strength, elastic behavior, and microfracture development during compression tests in granites. Eng Fract Mech 147:261–275

Hu X, Guo P, Xie N et al (2023) Creep behavior and associated acoustic characteristics of heterogeneous granite containing a single pre-existing flaw using a grain-based parallel-bonded stress corrosion model. Rock Mech Rock Eng 56(7):4799–4832

Ji Y, Zhuang L, Wu W, Hofmann H, Zang A, Zimmermann G (2021) Cyclic water injection potentially mitigates seismic risks by promoting slow and stable slip of a natural fracture in granite. Rock Mech Rock Eng 54(10):5389–5405

Kong L, Ranjith PG, Li BQ (2021) Fluid-driven micro-cracking behaviour of crystalline rock using a coupled hydro-grain-based discrete element method. Int J Rock Mech Min 144:104766

Lan H, Martin CD, Hu B (2010) Effect of heterogeneity of brittle rock on micromechanical extensile behavior during compression loading. J Geophys Res. https://doi.org/10.1029/2009JB006496

Lei B, Zuo J, Coli M et al (2024) Investigation on failure behavior and hydraulic fracturing mechanism of Longmaxi shale with different bedding properties. Comput Geotech 167:106081

Li BQ, Einstein HH (2019) Direct and microseismic observations of hydraulic fracturing in Barre Granite and Opalinus Clayshale. J Geophys Res Solid Earth 124(11):11900–11916

Li XF, Zhang QB, Li HB, Zhao J (2018) Grain-based discrete element method (GB-DEM) modelling of multi-scale fracturing in rocks under dynamic loading. Rock Mech Rock Eng 51(12):3785–3817

Li M, Wu J, Li J et al (2022) Modeling of hydraulic fracturing in polymineralic rock with a grain-based DEM coupled with a pore network model. Eng Fract Mech 275:108801

Li BQ, Moradian Z, Gonçalves Da Silva B, Germaine JT (2015) Observations of acoustic emissions in a hydraulically loaded granite specimen. In: 49th US rock mechanics/geomechanics symposium 2015

Liu G, Sun W, Lowinger SM, Zhang Z, Huang M, Peng J (2019) Coupled flow network and discrete element modeling of injection-induced crack propagation and coalescence in brittle rock. Acta Geotech 14(3):843–868

Naoi M, Chen Y, Yamamoto K et al (2020) Tensile-dominant fractures observed in hydraulic fracturing laboratory experiment using Eagle Ford Shale. Geophys J Int 222(2):769–780

Peng J, Wong LNY, Teh CI (2017) Influence of grain size heterogeneity on strength and microcracking behavior of crystalline rocks. J Geophys Res Solid Earth 122(2):1054–1073

Peng J, Wong LNY, Teh CI, Li Z (2018) Modeling micro-cracking behavior of Bukit Timah Granite using grain-based model. Rock Mech Rock Eng 51(1):135–154

Peng J, Wong LNY, Teh CI (2021) Influence of grain size on strength of polymineralic crystalline rock: New insights from DEM grain-based modeling. J Rock Mech Geotech Eng 13(4):755–766

Potyondy DO, Cundall PA (2004) A bonded-particle model for rock. Int J Rock Mech Min Sci 41:1329–1364

Potyondy DO (2010) A grain-based model for rock: approaching the true microstructure. In: Proceedings of rock mechanics in the Nordic Countries. pp. 9–12

Potyondy DO (2018) A flat-jointed bonded-particle model for rock. In: Proc 52nd US rock mechanics/geomechanics symposium; paper 12

Sagong M, Bobet A (2002) Coalescence of multiple flaws in a rock-model material in uniaxial compression. Int J Rock Mech Min Sci 39(2):229–241

Vallejos JA, Salinas JM, Delonca A, Ivars DM (2017) Calibration and verification of two bonded-particle models for simulation of intact rock behavior. Int J Geomech. https://doi.org/10.1061/(ASCE)GM.1943-5622.0000773

Wang T, Zhou W, Chen J, Xiao X, Li Y, Zhao X (2014) Simulation of hydraulic fracturing using particle flow method and application in a coal mine. Int J Coal Geol 121:1–13

Wang T, Hu W, Elsworth D et al (2017) The effect of natural fractures on hydraulic fracturing propagation in coal seams. J Petrol Sci Eng 150:180–190

Wang S, Zhou J, Zhang L, Nagel T, Han Z, Kong Y (2023) Modeling injection-induced fracture propagation in crystalline rocks by a fluid–solid coupling grain-based model. Rock Mech Rock Eng 56(8):5781–5814

Wang S, Potyondy DO, Chu W et al (2024) Investigation of meso-mechanical properties of Jinping dolomitic marble based on flat-joint model. J Rock Mech Geotech Eng. https://doi.org/10.1016/j.jrmge.2024.05.020. (**In press**)

Wong LNY, Einstein HH (2009a) Crack coalescence in molded gypsum and Carrara marble: part 2—microscopic observations and interpretation. Rock Mech Rock Eng 42(3):513–545

Wong LNY, Einstein HH (2009) Crack coalescence in molded gypsum and Carrara marble: part 1. Macroscopic observations and interpretation. Rock Mech Rock Eng 42(3):475–511

Wong LNY, Einstein HH (2009c) Systematic evaluation of cracking behavior in specimens containing single flaws under uniaxial compression. Int J Rock Mech Min 46(2):239–249

Wu SC, Xu XL (2016) A study of three intrinsic problems of the classic discrete element method using flat-joint model. Rock Mech Rock Eng 49(5):1813–1830

Zang A, Stephansson O (2010) Stress field of the earth's crust. Springer, Dordrecht

Zang A, Oye V, Jousset P, Deichmann N, Gritto R, McGarr A, Majer E, Bruhn D (2014) Analysis of induced seismicity in geothermal reservoirs—an overview. Geothermics 52:6–21

Zhang F, Dontsov E (2018) Modeling hydraulic fracture propagation and proppant transport in a two-layer formation with stress drop. Eng Fract Mech 199:705–720

Zhang F, Damjanac B, Huang H (2013) Coupled discrete element modeling of fluid injection into dense granular media. J Geophys Res Solid Earth 118(6):2703–2722

Zhang C, Ji H, You S, Geng Q (2024) A novel grain growth algorithm for grain-based models for investigating the complex behavior of crystalline rock. Comput Geotech 169:106230

Zhao X, Wang T, Elsworth D et al (2018) Controls of natural fractures on the texture of hydraulic fractures in rock. J Petrol Sci Eng 165:616–626

Zhao X, Elsworth D, He Y et al (2021) A grain texture model to investigate effects of grain shape and orientation on macro-mechanical behavior of crystalline rock. Int J Rock Mech Min 148:104971

Zhou Y, Lv W, Li B, Liang Q (2024) Impact of soft minerals on crack propagation in crystalline rocks under uniaxial compression: a grain-based numerical investigation. Int J Numer Anal Met. https://doi.org/10.1007/s12517-015-2196-6

Zhuang L, Zang A (2021) Laboratory hydraulic fracturing experiments on crystalline rock for geothermal purposes. Earth-Sci Rev 216:103580

Zhuang L, Kim KY, Jung SG, Diaz M, Min K (2019) Effect of water infiltration, injection rate and anisotropy on hydraulic fracturing behavior of granite. Rock Mech Rock Eng 52(2):575–589. https://doi.org/10.1007/s00603-018-1431-3

Zhuang L, Jung SG, Diaz M et al (2020) Laboratory true triaxial hydraulic fracturing of granite under six fluid injection schemes and grain-scale fracture observations. Rock Mech Rock Eng 53(10):4329–4344

Zhuang L, Zang A, Jung S (2022) Grain-scale analysis of fracture paths from high-cycle hydraulic fatigue experiments in granites and sandstone. Int J Rock Mech Min 157:105177